

# Dissolution in anisotropic porous media: Modelling convection regimes from onset to shutdown

Marco De Paoli,<sup>1,2,a)</sup> Francesco Zonta,<sup>1,b)</sup> and Alfredo Soldati<sup>1,2,3,c)</sup>

<sup>1</sup>*Institute of Fluid Mechanics and Heat Transfer, TU Wien, 1060 Vienna, Austria*

<sup>2</sup>*Dipartimento Politecnico, Università degli Studi di Udine, Udine 33100, Italy*

<sup>3</sup>*Department of Fluid Mechanics, CISM, Udine 33100, Italy*

(Received 4 October 2016; accepted 19 January 2017; published online 14 February 2017)

In the present study, we use direct numerical simulations to examine the role of non-isotropic permeability on solutal convection in a fluid-saturated porous medium. The dense solute injected from the top boundary is driven downwards by gravity and follows a complex time-dependent dynamics. The process of solute dissolution, which is initially controlled by diffusion, becomes dominated by convection as soon as fingers appear, grow, and interact. The dense solute finally reaches the bottom boundary where, due to the prescribed impermeable boundary, it starts filling the domain so to enter the shutdown stage. We present the entire transient dynamics for large Rayleigh-Darcy numbers,  $Ra$ , and non-isotropic permeability. We also try to provide suitable and reliable models to parametrize it. With the conceptual setup presented here, we aim at mimicking the process of liquid  $\text{CO}_2$  sequestration into geological reservoirs. *Published by AIP Publishing.* [<http://dx.doi.org/10.1063/1.4975393>]

## I. INTRODUCTION

When a heavier fluid is injected at the top of a porous slab, it is driven downward by gravity. After an initial diffusion transport, fingers appear and merge into convective plumes, whose strength and persistence depend on the magnitude of the driving force. If the bottom boundary is impermeable, the porous medium is eventually filled up by the liquid. The major proportion of this process is characterized by convective phenomena, from onset<sup>1,2</sup> (when convective overturning starts) to shutdown (when the filling process is being completed and convection cannot exist anymore). The dynamics described above has a fundamental importance in geological  $\text{CO}_2$  sequestration, since it faithfully mimics the process of liquid  $\text{CO}_2$  injection/transport in saline aquifers.<sup>3,4</sup> The injection of  $\text{CO}_2$  is realized at depths between 800 and 3000 m, where  $\text{CO}_2$  exists at a supercritical (liquid) state.<sup>5</sup> At the beginning,  $\text{CO}_2$  is lighter than brine and rises up until reaching an impermeable cap rock that stops the rising motion and favours a slower horizontal spreading. Under these conditions,  $\text{CO}_2$  has time to dissolve into the brine thereby increasing the density of brine. This new layer of dense saturated brine becomes rapidly unstable, so to foster the downward transport and the consequent deposition of  $\text{CO}_2$  at the bottom of the geological reservoir.

Therefore, the problem of  $\text{CO}_2$ -brine convection (solutal convection) described above shares some similarities with the thermal convection system (in a porous medium) characterized by two impermeable walls with prescribed temperature (Rayleigh-Bénard convection). However, it does display a

fundamental difference. In the classical Rayleigh-Bénard convection system, convective transport occurs away from both upper and lower boundaries and supports the existence of a statistically steady state, whose dynamics depends only on the value of the Rayleigh-Darcy number<sup>6-8</sup> ( $Ra$ ). In geological reservoirs, solutal convection is driven by a source of buoyancy occurring only at one boundary (the top one), a situation which induces a complex evolution characterized by a sequence of different regimes changing in time (time-dependent dynamics). In the initial stage, the dynamics develops only from the upper boundary, and the size of the system (or, in other words, the Rayleigh-Darcy number  $Ra$ ) is not influential until flow structures reach the opposite boundary. After this stage, the system starts depending on  $Ra$ . A comprehensive description of the above mentioned solutal convection in a porous medium has been recently proposed by Slim.<sup>9</sup> Through the use of accurate numerical simulations, Slim<sup>9</sup> extended previous experimental<sup>10,11</sup> and numerical<sup>12-14</sup> results found in the literature and was finally able to provide a unified picture of the entire dynamics for solute convection in an isotropic porous medium.

However, one important aspect for geological  $\text{CO}_2$  sequestration is rock anisotropy. Sedimentary rocks, which are composed by the subsequent accumulation of horizontal layers, are characterized by a horizontal permeability,  $k_h$ , that is larger compared to the vertical one,  $k_v$ . Hence the vertical-to-horizontal permeability ratio,  $\gamma = k_v/k_h$ , is typically  $\gamma < 1$ . Despite this fact, a larger proportion of the studies in this field consider the case of an isotropic porous medium ( $\gamma = 1$ ). There are only few works that focus on solutal convection in an anisotropic porous slab (see the work of Cheng *et al.*<sup>15</sup> and Green and Ennis-King,<sup>16</sup> among others). However, these studies were usually performed at lower  $Ra$  ( $Ra < 10^4$ ) and considered only the initial transient dynamics of the flow (they did not provide a detailed description of the entire

<sup>a)</sup>Email: [depaoli.marco@spes.uniud.it](mailto:depaoli.marco@spes.uniud.it)

<sup>b)</sup>Email: [francesco.zonta@tuwien.ac.at](mailto:francesco.zonta@tuwien.ac.at)

<sup>c)</sup>Author to whom correspondence should be addressed. Electronic mail: [alfredo.soldati@tuwien.ac.at](mailto:alfredo.soldati@tuwien.ac.at)

dissolution process dynamics). From the above considerations, it is apparent that a specific study accounting for the effect of  $\gamma$  on the entire solute dynamics at large  $Ra$  is still missing. We planned our work so to bridge the gap between the simulations of Slim<sup>9</sup> and those of Green and Ennis-King.<sup>16</sup> In particular, compared with the simulations of Slim<sup>9</sup> made for isotropic media and high  $Ra$ , we extended the analysis to the case of anisotropic media. Compared with the simulations of Green and Ennis-King<sup>16</sup> made for anisotropic media but at lower  $Ra$ , we completed the analysis extending it to higher  $Ra$  cases. Direct numerical simulations in anisotropic porous media at large  $Ra$  are used here to provide a unifying picture of solute dynamics in realistic geological reservoirs.

The paper is organized as follows: In Sec. II, the physical and numerical setup will be presented and discussed. In Sec. III, we will present the main results obtained from our simulations. We will characterize the entire solute dynamics, from the initial stages dominated by diffusion, up to the final shutdown stage. We will also provide parametrizations and suitable correlations for each stage of the solute dynamics. In Sec. IV, we will use our numerical results to develop a simple phenomenological model that provides a good estimate of the time required by the solute to fill the reservoir (shutdown time). We will finally draw conclusions and outline future developments.

## II. METHODOLOGY

We consider a porous medium in a two dimensional domain, where  $x^*$  is the horizontal direction and  $z^*$  the vertical direction. The porous medium, which is filled with CO<sub>2</sub> + brine mixture (solute) and pure brine (ambient fluid), is characterized by a uniform porosity  $\phi$  (fixed parameter between different simulations) and by different values of the vertical ( $k_v$ ) to horizontal ( $k_h$ ) permeability ratio  $\gamma = k_v/k_h$ . To represent physical geological situations, we choose  $1/2 \leq \gamma \leq 1$ .<sup>17</sup> At the beginning, the CO<sub>2</sub> concentration is zero everywhere but at the top boundary, where CO<sub>2</sub> is injected. As a consequence, the solute is driven by the composition-induced density difference in the vertical direction (with heavier fluid laying on top of lighter fluid) and is governed by a modified version of the Darcy's law written under the assumptions of the Oberbeck-Boussinesq approximation.<sup>18</sup> A natural reference velocity scale for this flow is the free-fall buoyancy velocity,  $W^* = gk_v\Delta\rho^*/\mu$ , with  $\mu$  the fluid viscosity,  $g$  the acceleration due to gravity, and  $\Delta\rho^*$  the initial top-to-bottom density difference of the solute. The corresponding reference length scale is  $h^* = \phi D/W^*$ , with  $D$  the solute diffusivity. To account for the effect of anisotropy, we use different velocity/length scales in the vertical and horizontal directions through the introduction of the scaling factor  $\sqrt{\gamma}$ . As a consequence, variables are made dimensionless as<sup>15</sup>

$$x = \frac{x^*}{h^*/\sqrt{\gamma}}, \quad z = \frac{z^*}{h^*}, \quad u = \frac{u^*}{W^*/\sqrt{\gamma}}, \quad w = \frac{w^*}{W^*}, \quad (1)$$

$$p = \frac{p^*}{\Delta\rho^*gh^*}, \quad C = \frac{C^*}{C_s^*}, \quad t = \frac{t^*}{\phi h^*/W^*}, \quad (2)$$

where  $t^*$  is time, and  $u^*$  and  $w^*$  are the velocities in the horizontal ( $x^*$ ) and vertical ( $z^*$ ) directions, whereas  $p^*$  and  $C^*$  are

pressure and solute concentration (with  $C_s^*$  the solute concentration at the top boundary). Note that the superscript  $*$  is used to represent dimensional quantities. The dependency of the fluid density with the concentration is given by the equation of state

$$\rho^* = \rho_s^* \left[ 1 - \frac{\Delta\rho^*}{\rho_s^* C_s^*} (C_s^* - C^*) \right], \quad (3)$$

with  $\rho_s^*$  the density at the top boundary. In the present study, we assume that the solute density is the only physical property that depends on concentration. This is a fair approximation for CO<sub>2</sub> + brine dissolving into pure brine.<sup>10,19</sup> By contrast, a different modelling approach should be used when considering CO<sub>2</sub> immersed in ambient brine. In this case, viscosity may change with solute concentration and may lead to important flow modifications.<sup>20</sup> Using the above scalings, the dynamics of the solute is described by the following set of dimensionless equations:

$$u = -\frac{\partial P}{\partial x}, \quad w = -\frac{\partial P}{\partial z} - C, \quad (4)$$

$$\frac{\partial u}{\partial x} + \frac{\partial w}{\partial z} = 0, \quad (5)$$

$$\frac{\partial C}{\partial t} + u \frac{\partial C}{\partial x} + w \frac{\partial C}{\partial z} = \gamma \frac{\partial^2 C}{\partial x^2} + \frac{\partial^2 C}{\partial z^2}, \quad (6)$$

with  $P = p + z(\rho_s^*/\Delta\rho^* - 1)$  the reduced pressure. Boundary conditions for the governing equations are as follows: the top boundary is an impermeable boundary characterized by a fixed solute concentration (mimicking the presence of a saturated solution near the top boundary), whereas the bottom boundary is an impermeable boundary for both the fluid and solute (i.e., no-flux boundary). Periodicity is applied at the side boundaries (along  $x$ ). In dimensionless form, these boundary conditions become

$$w = 0, \quad C = 1 \quad \text{for } z = 0, \quad (7)$$

$$w = 0, \quad \frac{\partial C}{\partial z} = 0 \quad \text{for } z = -Ra. \quad (8)$$

A sketch of the computational domain together with the indication of the boundary conditions and a contour map of the concentration  $C$  at a given time instant is shown in Fig. 1.

The main parameter of the simulation is the Rayleigh-Darcy number, which is the ratio of diffusive to convective time scales, defined as

$$Ra = \frac{gH^*k_v\Delta\rho^*}{\mu\phi D}, \quad (9)$$

where  $H^*$  represents the domain height. With the proposed scalings,  $Ra$  appears only in the boundary conditions (but not in the governing equations) and can be viewed as a dimensionless layer thickness. This clearly reveals that the value of  $Ra$  is not important until plumes impinge on the bottom boundary. Only after plumes impingement the presence of the bottom boundary is perceived by the entire fluid and  $Ra$  starts playing a major role on the subsequent dynamics.<sup>9</sup> Note that the effect of anisotropy ( $\gamma$ ) is explicit only in Eq. (6) but it is also present in the other equations through the reference length/velocity scales defined above. In the present study, we obtain  $\gamma < 1$  by increasing the horizontal permeability  $k_h$  while keeping  $k_v$  constant (i.e., keeping the same  $Ra$ ). Following this strategy, we are able to compare simulations at the same  $Ra$

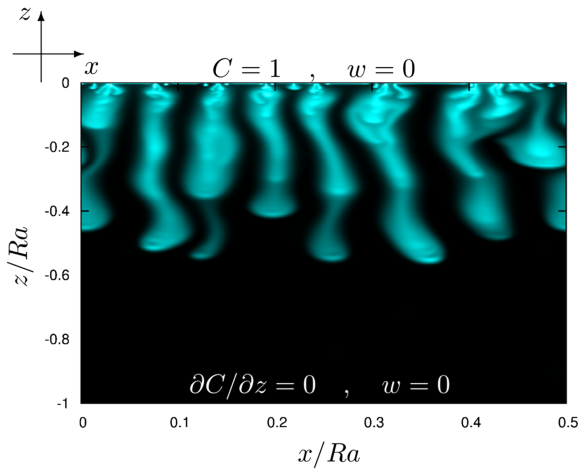


FIG. 1. Sketch of the computational domain with explicit indication of the boundary conditions (Eqs. (7) and (8)) employed. The contour map of the solute concentration  $C$  at a given time instant  $t$  is also shown to provide a flow visualization of the dynamics for the present physical configuration (injection of  $\text{CO}_2$  from the upper boundary).

(i.e., same driving force or same domain height) but different  $\gamma$  (i.e., different porous medium).

Governing equations (Eqs. (4)–(6)) have been solved through a pseudo-spectral Chebyshev-Tau method, which makes use of discrete Fourier transform in the horizontal direction, and Chebyshev polynomials in the vertical direction.

The time step,  $\Delta t = 1/2$ , has been chosen to ensure stability conditions. The spatial resolution ranges from  $2048 \times 513$  in the isotropic case to  $8192 \times 1025$  in the case of  $\gamma = 1/2$ . Further details on the numerical method can be found in the work of De Paoli *et al.*,<sup>8</sup> Zonta and Soldati,<sup>21</sup> and Zonta *et al.*<sup>22</sup>

### III. RESULTS

In this section, we discuss the results obtained from our numerical simulations of the concentration-driven  $\text{CO}_2$  dissolution process in geological reservoirs. As in previous works,<sup>9</sup> we assume as initial condition the diffusive concentration profile

$$C(z, t) = 1 + \operatorname{erf}\left(\frac{z}{\sqrt{4t}}\right) \quad (10)$$

perturbed with a random noise. In particular, we follow the entire time-dependent dynamics of the flow field for a given  $Ra$  number ( $Ra = 2 \times 10^4$ ) and different values of  $\gamma$  ( $\gamma = 1, 3/4$ , and  $1/2$ ). The value of  $Ra$  has been inspired by the data referring to the geological reservoir of the Sleipner site (North Sea). Following the work of Bickle *et al.*<sup>23</sup> and Neufeld *et al.*,<sup>10</sup> we assume a porous layer (domain) having  $H^* \approx 20$  m,  $k_v = 4 \times 10^{-12}$  m<sup>2</sup>, and  $\phi = 0.375$ . At the typical depth of solute injection, the fluid properties are<sup>12</sup>  $\Delta\rho = 10.45$  kg/m<sup>3</sup>,  $\mu = 5.95 \times 10^{-4}$  Pa s, and  $D = 2 \times 10^{-9}$  m<sup>2</sup>/s, which finally give a Rayleigh-Darcy number  $Ra \approx 1.8 \times 10^4$ .

We start our discussion considering the case of an isotropic porous medium ( $Ra = 2 \times 10^4$ ,  $\gamma = 1$ ). We will briefly discuss the different flow regimes observed in the present computation, since some of these observations will be useful in the following while discussing the effects of  $\gamma$  on the solute dynamics.

The entire time-dependent solute dynamics is made of six consecutive regimes. At the beginning, solute transport occurs from the upper boundary only (where  $\text{CO}_2$  is injected) and is essentially dominated by solute diffusion: a diffusion (i) and a linear-growth regime (ii) are here observed. Later, small fingers form, grow, interact, and merge into megaplumes so to enter a long transient phase dominated by convection. Three different regimes are now encountered: flux growth (iii), merging (iv), and constant flux regimes (v). Finally, megaplumes reach the bottom boundary (which is impermeable for both the fluid and solute), and the reservoir starts filling up with dense solute: the flow enters the so-called shutdown regime (vi).

A comprehensive picture of the entire time-dependent flow dynamics just drafted above is shown in Fig. 2. The central panel of this figure (Fig. 2(b)) presents the behaviour of the solute flux  $F(t)$  as a function of time. The dashed lines represent the analytical prediction of  $F(t)$  found in the literature for the different flow regimes; the extensions of which are explicitly indicated as well (further details on the different scalings and analytical expressions will be explicitly given in Secs. III A–III C). Associated with the changes of  $F(t)$  in time, we expect a modification of the flow structure. This is clearly shown in Figs. 2(a)–2(c), where the time evolution of the concentration  $C$  measured along a horizontal slice located close to the top wall is plotted. This provides a good representation for the behaviour of plumes in time. In particular, we note that diffusion dominates for  $t < 10^3$  (Fig. 2(a)), with plumes appearing only at the end of the linear growth regime (emergence of dark roots at  $t \approx 10^3$  in Fig. 2(a)). For  $t > 10^3$ , plumes start interacting (merging and constant flux regimes in Fig. 2(a)). Later, during the constant flux regime and for most of the shutdown regime, the dominating dynamics consists of small protoplumes (small ribs in Fig. 2(c)) generated at the wall and merging into larger megaplumes (long roots in Fig. 2(c)). Note that during the shutdown regime, the relative strength of protoplumes and megaplumes compared to the surrounding flow decreases with time (flow homogenization for  $t > 10^5$ , Fig. 2(c)). The above dynamics of solute convection in an isotropic porous medium has been widely investigated from both the numerical and the experimental point of view.<sup>9,10,12,13</sup> However, it has been only slightly characterized for a non-isotropic porous medium.<sup>15,16,24</sup>

In the following, we try to fill this gap, discussing the effect of  $\gamma$  on the solute dynamics. We will recast the entire dynamics into three main stages: a diffusion dominated stage (including diffusion and linear growth), a convective dominated stage (including flux growth, merging, and constant flux), and a shutdown stage (shutdown).

#### A. The diffusion-dominated stage

As already discussed, upon injection from the top boundary, the solute moves downwards by diffusion. Since solute diffusion is very slow, the bottom boundary can be considered sufficiently far from the top boundary during this stage. Therefore, we can approximate the bottom boundary conditions as

$$w = 0, \quad C \approx 0 \quad \text{at} \quad z = -Ra. \quad (11)$$

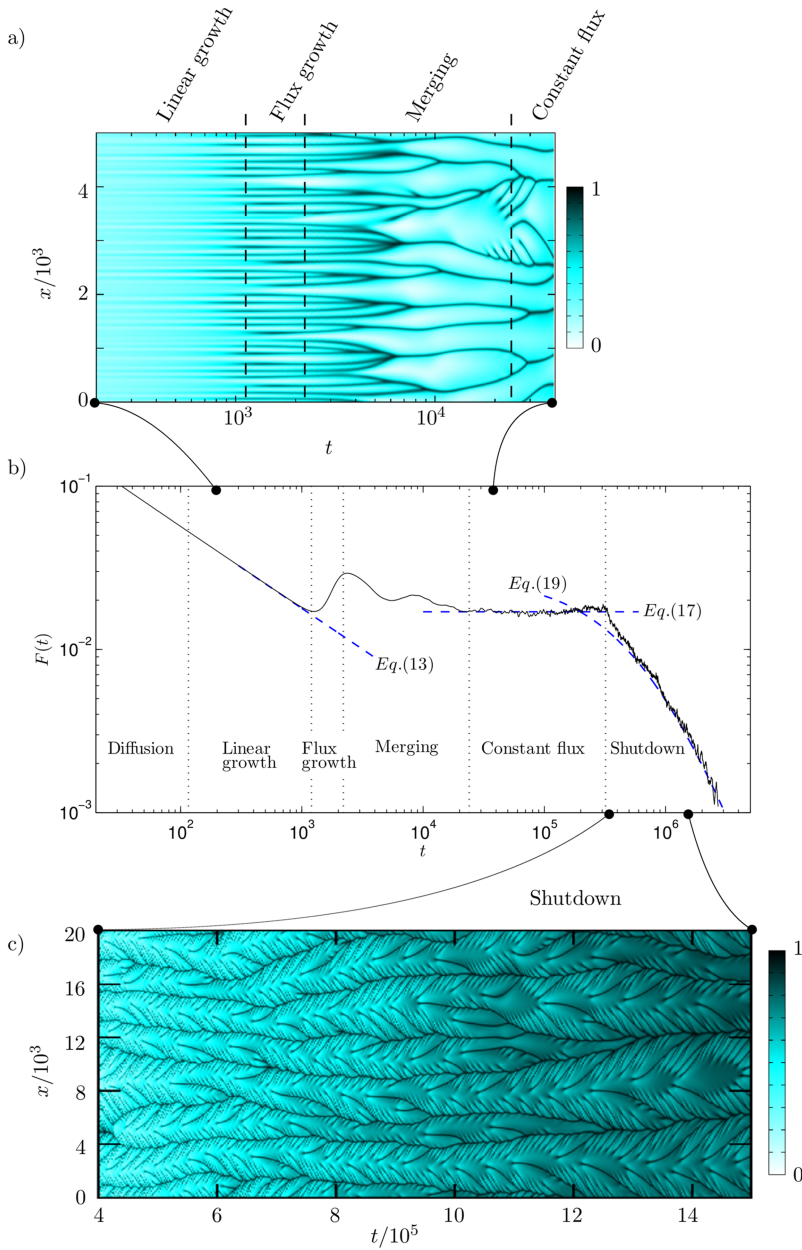


FIG. 2. Time behaviour of the solute dissolution for  $Ra = 2 \times 10^4$  and  $\gamma = 1$ . Main panel (panel (b)): dissolution flux  $F(t)$  as a function of time. Solid line refers to the present numerical simulation. Dashed lines indicate analytical predictions found in the literature for the diffusion regime ( $t < 10^3$ , Eq. (13)); the constant flux regime ( $2 \times 10^4 < t < 2 \times 10^5$ , Eq. (17)); and the shutdown regime ( $2 \times 10^5 < t < 3 \times 10^6$ , Eq. (19)). The formulation of these theoretical predictions is explicitly given in the text (Sec. III). Note that the extent of the different flow regimes is also explicitly indicated. Side panels (panels (a) and (c)): time behaviour of the concentration field measured along an horizontal slice ( $x$ ) located close to the top wall ( $z = -20$  for panel (a),  $z = -50$  for panel (c)) measured for different time windows during the transient evolution (panel (a) refers to  $2 \times 10^2 \leq t \leq 4 \times 10^4$ , whereas panel c refers to  $4 \times 10^5 \leq t \leq 15 \times 10^5$ ).

Within this framework, the solution of Eq. (6) yields

$$C(z, t) = 1 + \operatorname{erf}\left(\frac{z}{\sqrt{4t}}\right), \quad (12)$$

with the dimensionless solute flux being

$$F(t) = \frac{1}{L} \int_0^L \left. \frac{\partial C}{\partial z} \right|_{z=0} dx = \frac{1}{\sqrt{\pi t}}, \quad (13)$$

where  $L$  is the dimensionless domain width. The corresponding amount of solute dissolved in time,  $G(t)$ , is given by the integral of the solute flux  $F(t)$ ,

$$G(t) = \int_0^t F(\tau) d\tau = \frac{2\sqrt{t}}{\sqrt{\pi}}. \quad (14)$$

The profiles of  $F(t)$  and  $G(t)$  obtained from the present computations are shown in the two panels of Fig. 3 for  $Ra = 2 \times 10^4$  and different values of  $\gamma$  (symbols in Fig. 3). The dashed line

in Fig. 3 indicates the analytical prediction given by Eq. (13). We first consider Fig. 3(a). For  $t < 10^3$ , we observe that the behaviour of  $F(t)$  is independent of  $\gamma$  and follows nicely the theoretical predictions. Later in time, at  $t = t_{on}$  (onset time of convection), convection is triggered and the profile of  $F(t)$  departs from the theoretical prediction of a pure diffusive flow. In the literature, there are different expressions to find the value of  $t_{on}$  as a function of  $\gamma$ ,<sup>16</sup> essentially because  $t_{on}$  depends on the initial conditions prescribed in the simulations. To predict the value of  $t_{on}$ , we follow the expression of Cheng *et al.*,<sup>15</sup>

$$t_{on} = 47.9\gamma^{0.79}. \quad (15)$$

In the present cases, we obtain  $t_{on} = 47.9$  ( $\gamma = 1$ ),  $t_{on} = 38$  ( $\gamma = 3/4$ ), and  $t_{on} = 27$  ( $\gamma = 1/2$ ). The departure of  $F(t)$  from the purely diffusive profile for  $t > t_{on}$  is barely visible at the beginning. Well beyond  $t_{on}$ , at time  $t = t_d$ , diffusion is balanced by convection and the dissolution flux reaches a minimum. We

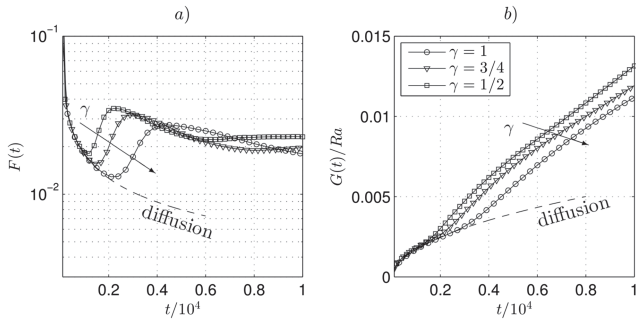


FIG. 3. (a) Solute dissolution flux  $F(t)$  vs time  $t$  in the early stages of the simulations, plotted for  $Ra = 2 \times 10^4$  and  $\gamma = 1/2, 3/4$ , and 1. The dashed line represents the dissolution flux computed as in Eq. (13). (b) Total solute dissolved from  $t = 0$  for the different permeability ratios considered (solid lines) and from the theory (Eq. (14)). We report the same simulations presented in (a), and the lower the permeability ratio, the sooner the flux deviates from diffusion.

further remark here that there is a large difference between  $t_{on}$  and  $t_d$  ( $t_d$  is on average two orders of magnitude larger than  $t_{on}$ ). The decrease of  $\gamma$  (i.e., the increase of the horizontal permeability) reduces the value of  $t_d$  (and also of  $t_{on}$ ), indicating that convection is triggered early when  $\gamma < 1$ . In particular, we found  $t_d \approx 2.2 \times 10^3$  ( $\gamma = 1$ ),  $t_d \approx 1.6 \times 10^3$  ( $\gamma = 3/4$ ), and  $t_d \approx 1.1 \times 10^3$  ( $\gamma = 1/2$ ). Just after  $t_d$ , the dissolution flux increases sharply. For this reason,  $t_d$  is sometimes taken as a practical measure of the onset time of convection. From a phenomenological point of view, after  $t_d$  fingers become visible and start transporting efficiently dense solute away from the boundary, so to increase the dissolution flux. Fingers are at first characterized by negligible lateral movements (see also the regular, and parallel, footprint of fingers during the flux growth regime in Fig. 2). Later, fingers increase their length and strength and start modifying the entire velocity field. This causes fingers to come closer and eventually merge with the neighbours (as also shown by the evolution of the finger roots during the merging regime in Fig. 2(a)) to create larger plumes. The merging process decreases the number of plumes and increases the boundary layer thickness, hence reducing the dissolution flux (decrease of  $F(t)$  for  $t > 0.2 \times 10^4$  in Fig. 3). By looking at the behaviour of  $G(t)$  in Fig. 3(b), one important observation can be made. After the initial transient where  $G(t)$  follows the pure diffusional profile (regardless of the value of  $\gamma$ ), we note that solute dissolution appears more efficient for decreasing  $\gamma$ . At  $t = 10^4$ , the amount of solute dissolved for  $\gamma = 1/2$  can be up to 20% larger compared to  $\gamma = 1$ .

## B. The convection-dominated stage

After the initial diffusive dynamics, the flow enters a convection dominated stage called constant flux regime.<sup>9,25,26</sup> During this regime, primary plumes already generated in the previous stages of the flow rapidly grow. At the same time, the diffusive boundary layer between adjacent plumes becomes unstable and continuously produces new protoplumes. The newly formed protoplumes are driven laterally by the background flow and coalesce with primary plumes. During this stage, the average flux of solute fluctuates around a mean constant value (Fig. 4). For isotropic conditions ( $\gamma = 1$ ), we

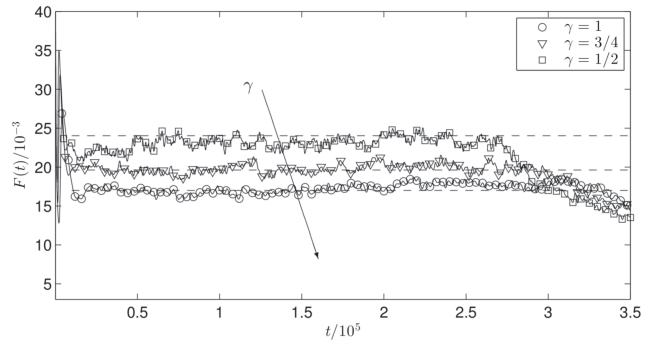


FIG. 4. Constant flux regime. Dimensionless solute flux  $F(t)$  for three different permeability ratios ( $1/2, 3/4$ , and 1) at fixed Rayleigh number ( $Ra = 2 \times 10^4$ ). In the constant flux regime, the simulations (solid lines) are in good agreement with the predictions of Green and Ennis-King<sup>16</sup> (dashed lines).

recover the value  $F(t) = 1.7 \times 10^{-2}$  proposed by Pau *et al.*,<sup>12</sup> Slim,<sup>9</sup> and Hesse,<sup>27</sup> among others. The dimensional solute flux can be expressed as<sup>10,16</sup>

$$F^*(t^*) = 0.017 \sqrt{k_h k_v} \frac{C_s^* \Delta \rho^* g}{\mu} \quad (16)$$

or, in dimensionless form,

$$F(t) = 0.017 \gamma^{-1/2}. \quad (17)$$

The theoretical predictions given by Eq. (17) are shown by the dashed lines (—) in Fig. 4. We note a fair agreement between numerical results (symbols) and theoretical predictions (dashed lines), which demonstrates for the first time that the scaling law proposed in the literature<sup>16</sup> for lower values of  $Ra$  ( $10^3 \leq Ra \leq 9 \times 10^3$ ) can be extended up to  $Ra = 2 \times 10^4$ , as shown by the present results. Note that, although the time at which the constant flux regime starts does depend on the initial conditions of the flow, the average value of the dissolution rate  $F(t)$  in the constant flux regime does not.<sup>9</sup> This indicates also that the constant flux regime and the final shutdown regime are universal stages in which the effects of different initial conditions are only chaotic fluctuations around the average behaviour. Therefore, the corresponding parametrization (presented in this section and in Sec. III C) is universal and does not depend on the specific initial conditions. We wish to remark here that this dynamics does not change substantially in 3D domains. The main difference between 2D and 3D results is that the time fluctuation of  $F(t)$  around its average value is large for 2D rather than for 3D cases.<sup>12</sup> This was also observed by Hewitt *et al.*,<sup>28</sup> using different boundary conditions (i.e., Dirichlet type boundary conditions at both top and bottom boundaries).

## C. The shutdown stage

Once the plumes reach the bottom boundary, the domain starts filling up with dense solute and the flow enters the last stage of its dynamics, usually called the shutdown stage. Despite its practical importance, the shutdown stage in non-isotropic porous media has never been explicitly computed, with the only available predictions<sup>8</sup> being based on extrapolations from different flow configurations (different boundary conditions at the bottom wall). In the present paper,

we explicitly compute the solute dynamics in the shutdown regime for  $\gamma < 1$ . This has never been done before. Results are shown in Fig. 5. Symbols in Fig. 5(a) refer to the behaviour of  $F(t)$  for  $\gamma = 1$ . These results are obtained running four different simulations with different initial random perturbations, and averaging the corresponding results to observe a smoother profile. The dashed line represents the theoretical prediction of  $F(t)$  based on numerical results for the two-sided configuration.<sup>8</sup> We briefly recall here that these theoretical predictions prescribe that  $F(t)$  depends on the permeability ratio  $\gamma$  and on the convective time scale  $\hat{t} = \phi H^*/W^*$  as

$$F^*(t^*) = \frac{4\alpha\gamma^n \hat{t}}{(\hat{t} + 4\alpha\gamma^n t^*)^2} H^* \phi C_s^*, \quad (18)$$

with  $\alpha = 0.00688$  and  $n = -0.25$ . Upon rescaling this expression with the present length and time scales, we obtain the following behaviour for the dimensionless dissolution flux  $F(t)$ :

$$F(t) = \frac{4\alpha\gamma^n}{(1 + 4\alpha\gamma^n t/Ra)^2}. \quad (19)$$

For  $\gamma \rightarrow 1$ , Eq. (19) tends to the expression given by Hewitt *et al.*<sup>13</sup> First note that the temporal extension of the shutdown stage ( $O(10^6)$ ) is at least an order of magnitude larger than that of the previous stages ( $O(10^5)$ ). We clearly observe that the prediction obtained using the theoretical model follows nicely the numerical simulations, but during the transition of the flow from the constant flux to the shutdown regime, up to  $t \approx 4 \times 10^5$ . The source of this discrepancy lies on the model hypothesis of having a well mixed  $C(t)$  profile, which is not fulfilled during this transition. The corresponding behaviour of the solute dissolved in time during the shutdown stage,  $G(t)$ , is shown in the inset of Fig. 5(a) for  $\gamma = 1$ . As expected,  $G(t)$  increases sharply at the beginning and levels for larger times, due to the ongoing weakening of convection. To highlight the role of  $\gamma$  on the dynamics of the shutdown regime, in Fig. 5(b) we show the behaviour of the normalized difference  $G(\gamma)/G(1) - 1$  between the solute dissolved for  $\gamma \neq 1$  and that dissolved for  $\gamma = 1$ . We clearly observe that the amount of solute dissolved for  $\gamma \neq 1$  can be definitely larger (up to 25% for  $\gamma = 1/2$ ) than that dissolved for  $\gamma = 1$ . Note that this difference increases for decreasing  $\gamma$ . As expected, in the long term limit ( $t > 20 \times 10^5$ ), the solute dissolved depends only on the available volume but not on  $\gamma$  (i.e.,  $\lim_{t \rightarrow \infty} [G(\gamma)/G(1) - 1] = 0$ ).

From the discussion presented above, it is apparent that most of the solute dissolution occurs during the constant flux and the shutdown regime (they cover a large proportion of the dynamics,  $t > 2 \times 10^4$ ). For this reason, deriving simple and reliable models of these two regimes based on accurate small-scales simulations is crucial for the development of numerical tools for the prediction of the solute dynamics in realistic applications (large scale reservoirs with non-isotropic permeability). This will be accomplished in Sec. IV.

#### IV. MODEL DEFINITION

In Sec. III, we have revisited the available models found in the literature<sup>8,9,13,16</sup> to describe the solute dissolution in geological reservoirs having non-isotropic rock permeability. From the present study, we propose the following parametrization of the solute flux  $F(t)$  for  $\gamma < 1$ :

$$F(t) = \begin{cases} 1/\sqrt{\pi t}, & 0 \leq t < t_1 \\ 0.017\gamma^{-1/2}, & t_1 \leq t < t_2 \\ 4\alpha\gamma^n/(1 + 4\alpha\gamma^n t/Ra)^2, & t_2 \leq t < +\infty \end{cases}, \quad (20)$$

where  $t_1$  and  $t_2$  represent the time at which the constant flux and the shutdown regimes start, respectively. We wish to remark here that the present parametrization is a generalization of previous literature models,<sup>9,13,16</sup> yet satisfying such models for isotropic, high- $Ra$  number flows<sup>9,13</sup> and for anisotropic, intermediate- $Ra$  number flows.<sup>16</sup> Although the expression of  $F(t)$  is well defined for the different regimes, the time instants at which the different regimes start and finish still remain unclear. To resolve this problem, we propose the following reasoning.

At the beginning, the entire domain is fully saturated with pure brine, such that

$$C^*(x, z \neq 0, t = 0) = 0 \quad \forall x. \quad (21)$$

At  $t > 0$ ,  $\text{CO}_2$  is injected from the top boundary and the domain starts filling up with dense solute. The maximum quantity of solute that can be dissolved is given by the available volume of the reservoir per unit depth,  $\phi H^*$ , multiplied by the concentration of the saturated upper boundary  $C_s^*$ . The amount of solute dissolved from time zero to time  $t^*$ ,  $G^*(t^*)$  [ $\text{kg}/\text{m}^2$ ], is

$$G^*(t^*) = \int_0^{t^*} F^*(\tau^*) d\tau^*. \quad (22)$$

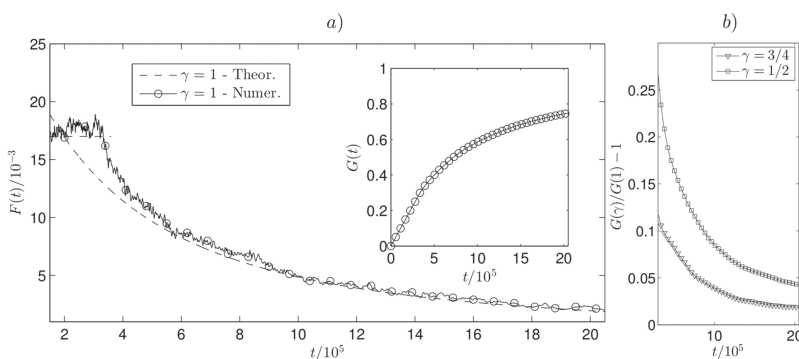


FIG. 5. (a) Time behaviour of the solute dissolution flux  $F(t)$  for  $Ra = 2 \times 10^4$  and  $\gamma = 1$  ( $- \circ -$ ) during the shutdown regime (and including also a small part of the constant flux regime,  $t < 4 \times 10^5$ ). The theoretical prediction given by the model of De Paoli *et al.*<sup>8</sup> is also shown (dashed line,  $- -$ ). The amount of solute dissolved in time,  $G(t)$ , is shown in the inset for  $\gamma = 1$ . (b) Time behaviour of the normalized amount of solute  $(G(\gamma) - G(1))/G(1)$  dissolved for  $\gamma = 1/2$  and  $\gamma = 3/4$  during the shutdown regime.

Upon rescaling of  $G^*$  by  $\phi C_s^* H^*$ , we have<sup>8</sup>  $G(t \rightarrow +\infty) = Ra$ . This imposes a constraint for the dimensionless flux  $F(t)$ , since

$$\int_0^{+\infty} F(\tau) d\tau = Ra. \quad (23)$$

Neglecting the contribution of the flux growth and merging regimes to the solute dissolution process (these two regimes are short in time, depend on the initial condition, and are hard to parametrize<sup>9</sup>), and using the expression summarized in Eq. (20) for  $F(t)$ , we obtain

$$\frac{2}{\sqrt{\pi}} \sqrt{t_1} + 0.017\gamma^{-1/2}(t_2 - t_1) + \frac{Ra}{1 + 4\alpha\gamma^n t_2/Ra} = Ra. \quad (24)$$

From both literature predictions<sup>9</sup> and present results, we have  $t_1 = O(10^3)$ . We can easily show that, for large  $Ra$ , the amount of solute dissolved during diffusion,  $G = O(10)$ , is negligible compared to the total amount of solute dissolved in the entire dissolution process,  $G(\infty) = Ra = O(10^4)$ . Therefore, assuming  $t_1 \rightarrow 0$  in Eq. (24), we obtain

$$\frac{t_2}{Ra} = \left( \frac{4\alpha\gamma^n}{0.017\gamma^{-1/2}} - 1 \right) \frac{1}{4\alpha\gamma^n}, \quad (25)$$

which gives  $t_2/Ra(\gamma = 1) = 22.6$ . According to this result, the shutdown time  $t_2$  is much larger than the expected one, i.e.,  $15\text{--}16 \times Ra$ , see also the work of Hewitt *et al.*<sup>13</sup> and Slim.<sup>9</sup> As already mentioned, the difference between theoretical and numerical predictions of the shutdown time is due to the behaviour of the solute concentration during the transition from the constant flux regime to the shutdown regime. During this transition, the assumption of having a well-mixed concentration profile used to derive the model<sup>8</sup> is not fulfilled. This is apparent in Fig. 6, where the solute concentration in the domain is explicitly shown at different times (from P1 to P4). The distribution of  $C$  is definitely not uniform for P1, P2, and P3 (hence the concentration profile is not uniform, i.e., solute

is not well-mixed), whereas it becomes more homogeneous for P4 (solute is well-mixed). In an effort to obtain a more precise estimate of the time at which the shutdown regime starts ( $t_2$ ), we should model the time evolution of the concentration profile during the transition between the constant flux regime and the shutdown regime. From the results of our numerical simulations (Fig. 7(a)), we observe that the horizontally averaged concentration profile at a certain time instant  $t$  during the constant flux regime,  $\bar{C}(z, t) = 1/L \int_L C(x, z, t) dx$ , exhibits an almost linear variation along the vertical coordinate  $z$  (see the solid line in Fig. 7(a)). Therefore,  $\bar{C}(z, t)$  can be expressed as

$$\bar{C}(z, t) = -\frac{C_1(t)}{z_1(t)} [z - z_1(t)], \quad (26)$$

with  $z_1 \leq z \leq 0$  for any  $t$ . The linear prediction of  $\bar{C}(z, t)$  given by Eq. (26) is also shown in Fig. 7(a) (dashed line, - -) together with the numerical results. To determine the value of the two constants of the model ( $C_1$  and  $z_1$ , which in general do depend on time), we use the following constraints. At the beginning ( $t = 0$ ), the domain is solute-free (fully saturated with pure brine). At  $t > 0$ ,  $\text{CO}_2$  is injected from the top boundary. Therefore, the amount of solute dissolved from time  $t > 0$  up to time  $t$  is equal to the amount of solute contained in the volume  $V$  at time  $t$ ,

$$\int_0^t \left( \int_L \frac{\partial C(x, z, \tau)}{\partial z} \Big|_{z=0} dx \right) d\tau = \int_V C(x, z, t) dV. \quad (27)$$

Eq. (27) can be integrated using Eq. (26) (to express  $C(x, z, t)$ ) and Eq. (17) (to express  $\partial C(x, z, \tau)/\partial z$ ) to give

$$C_1(t)z_1(t) = -0.034\gamma^{-1/2}t. \quad (28)$$

From our numerical simulations, we observe that  $C_1(t)$  (that is the position at which the concentration starts showing a linear dependence on  $z$ , see Fig. 7(a)) is almost constant with time, regardless of the value of  $\gamma$ . In particular, we found

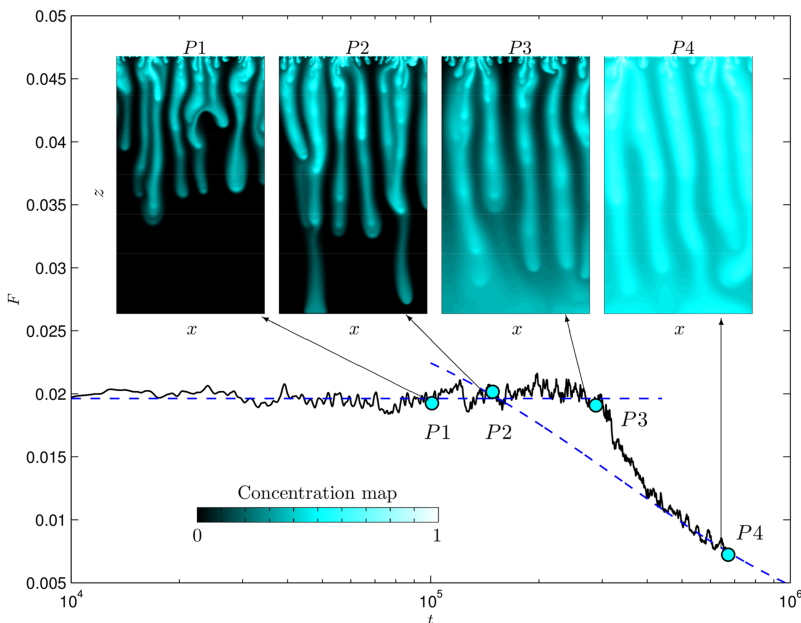


FIG. 6. Transition phase between the constant flux and the shutdown regime. Solid line (—) indicates the time evolution of the dissolution flux  $F(t)$ , whereas the dashed lines (---) correspond to the theoretical predictions given by the models (see Eqs. (17) and (19)). Four different snapshots of the solute concentrations are also shown. In P1, plumes are far from the bottom boundary (constant flux); plumes reach the bottom boundary in P2; later, the domain starts filling up with dense solute (P3) until convection shutdown (P4).

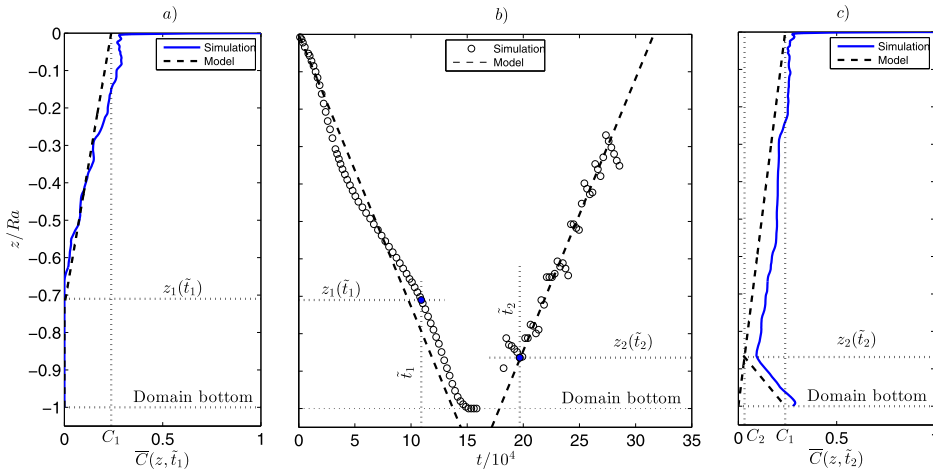


FIG. 7. Panels (a) and (c): Horizontally averaged concentration profile  $\bar{C}$  computed at  $\bar{t}_1 \approx 11 \times 10^4$  and  $\bar{t}_2 \approx 19 \times 10^4$ . The profiles obtained from the simulation ( $\gamma = 3/4$ , solid lines) are plotted against the model (dashed lines). Panel (b) the “averaged plume tip”  $z_1(t)$  (left side) and the local concentration minimum (right side) are plotted. The values obtained from the simulations (circles) are well approximated from the model (dashed line). The filled circles represent the instants related to the left and right panel profiles. Application of the model to other values of  $\gamma$  gives similar results (not shown here).

$0.21 < C_1 < 0.26$  for  $1/2 \leq \gamma \leq 1$ . This information on  $C_1$  can be used, together with Eq. (28) to obtain the value of  $z_1$ , which can be seen as the position of the wavefront of a falling solutal wave (or as the averaged tip position of falling plumes). Therefore the wavefront moves downward at a constant speed  $\partial z_1 / \partial t = w = -0.034\gamma^{-1/2} / C_1$ . For  $\gamma = 1$ ,  $C_1 = 0.21$  and  $w = -0.16$ , in fair agreement with the results obtained by Slim<sup>9</sup> ( $C_1 = 0.27$  and  $w = -0.13$ ). Note that the constant speed of the solutal wavefront, which is a consequence of the linear behaviour adopted in the model, is also supported by the present numerical results. To demonstrate this, in Fig. 7(b), we plot the time behaviour of  $z_1$  obtained from simulations (symbols,  $\circ$ ), together with the theoretical behaviour (dashed line,  $--$ ) obtained for a constant velocity profile (i.e., a linear variation of  $z_1$  with  $t$ ). Although some discrepancies between numerical and analytical results are present, the agreement is satisfactory and demonstrates the reliability of the model.

After the plumes reach the bottom boundary, the solute concentration  $C$  increases from bottom to top. During this stage, the concentration profile  $\bar{C}(z, t)$  has a bilinear shape (see Fig. 7(c)). When the solute wavefront reaches the bottom ( $t = t_b$ ), we have

$$\bar{C}(z, t_b) = \frac{z + Ra}{Ra} C_1. \quad (29)$$

For  $t > t_b$ , after an initial redistribution phase during which  $C$  fluctuates at the bottom boundary, we can assume that the solute wavefront bounces back and moves upwards with the same average velocity of the falling phase,  $w$ , but opposite sign. We also assume that the concentration at the bottom boundary is fixed and equal to  $C_1$  (this is in fair agreement with the results of the simulations, see the solid line in Fig. 7(c)). From this assumptions, we find that the position of the kink of the concentration profile ( $z_2(t)$  in Fig. 7(c)) moves upward from  $z_2 = -Ra$  until  $z_2 = 0$  as

$$z_2(t) = -Ra - w[t - (1 + \eta)t_b]. \quad (30)$$

Note that  $\eta$  is a parameter accounting for the redistribution phase of solute after the first impact of the wavefront on the bottom boundary. For  $\gamma = 1$ ,  $3/4$ , and  $1/2$ , the parameter  $\eta$  results to be 0.4, 0.3, and 0.2, respectively. This reflects the physical intuition that the smaller is  $\gamma$  (larger  $k_h$ , i.e., smaller horizontal resistance to the flow), the shorter the redistribution

phase. Using the bilinear model, we are able to predict the shutdown time  $t_2$  (i.e., the time the solute wavefront takes to reach the bottom boundary and back to the top one),

$$t_2 = \frac{(2 + \eta) Ra}{|w|} = \frac{(2 + \eta) C_1}{0.034\gamma^{-1/2}} Ra. \quad (31)$$

For the isotropic case ( $\gamma = 1$ ,  $C_1 = 0.21$ , and  $\eta = 0.4$ ), we have  $t_2 \approx 15 \times Ra$ , in good agreement with literature results<sup>9,13</sup>  $15$ – $16 \times Ra$ . The shutdown time predicted by Eq. (31), presented here for the first time, accounts for the effect of anisotropy on the fluid redistribution after plume impingement (via the parameter  $\eta$ ) and gives more accurate results compared to those given by Eq. (25).

We finally note that the shutdown time predicted by Eq. (31) reduces for reducing  $\gamma$ . This is also supported by the present numerical results (see the different times at which the profile starts decreasing in Fig. 4).

## V. CONCLUSIONS AND FUTURE DEVELOPMENTS

In this work, we focused on the transient dynamics of solute convection in a two-dimensional anisotropic porous medium. The gap existing between the knowledge of solutal regimes in isotropic<sup>9</sup> and in anisotropic<sup>16</sup> porous media at large Rayleigh number has been investigated. Dense solute, which was initially injected from the top boundary, was driven down by gravity and finally accumulated at the bottom impermeable boundary. With this conceptual setup, we aimed at mimicking the process of liquid  $\text{CO}_2$  sequestration in realistic geological reservoirs.

With the aid of accurate numerical simulations, we characterized and discussed the entire solute dynamics at high Rayleigh-Darcy number ( $Ra = 2 \times 10^4$ ), from the initial diffusion-dominated stage up to the final convection-dominated and shutdown stages. The role of the anisotropic flow permeability ( $\gamma$ ) throughout the entire process was singled out. For the first time, we were able to provide a unifying picture of the solute dynamics in realistic geological reservoirs. Compared to the isotropic case ( $\gamma = 1$ ), solute convection is triggered early when  $\gamma < 1$  and solute dissolution appears in turn more efficient. In particular, we observe that the finite-time amount (short-term limit) of solute dissolved and stored inside

the reservoir is larger for decreasing  $\gamma$  (up to 25% for  $\gamma = 1/2$ ). As expected, in the long-term limit (asymptotic behaviour), the amount of solute dissolved depends only on the available volume but not on  $\gamma$ .

Based on our current original results obtained for  $\gamma < 1$ , simplified theoretical models used to predict the value of the solute flux,  $F(t)$ , throughout the entire dissolution process have also been developed. These small-scale models can be easily nested into larger scale models to obtain accurate predictions of the dissolution flux in realistic applications, where heterogeneities and anisotropies are inherently present.

Further steps of this study will be the description of the solute dissolution process of a given amount of solute in a close reservoir characterized by impermeable conditions for both the fluid and solute on either the top and the bottom walls. In this case, a more sophisticated approach describing the dynamics of two immiscible (or partially miscible) species could be developed and applied.

## ACKNOWLEDGMENTS

We gratefully acknowledge CINECA Supercomputing center for the availability of computational resources. The computational results presented have also been achieved using the Vienna Scientific Cluster (VSC-3). M.D. gratefully acknowledges financial support from Project No. 2015-1-IT02-K103-013256 funded by UE Erasmus.

- <sup>1</sup>C. W. Horton and F. T. Rogers, Jr., "Convection currents in a porous medium," *J. Appl. Phys.* **16**(6), 367–370 (1945).
- <sup>2</sup>E. R. Lapwood, "Convection of a fluid in a porous medium," *Proc. Cambridge* **44**, 508–521 (1948).
- <sup>3</sup>D. Bolster, "The fluid mechanics of dissolution trapping in geologic storage of CO<sub>2</sub>," *J. Fluid Mech.* **740**, 1–4 (2014).
- <sup>4</sup>M. L. Szulczewski, M. A. Hesse, and R. Juanes, "Carbon dioxide dissolution in structural and stratigraphic traps," *J. Fluid Mech.* **736**, 287–315 (2013).
- <sup>5</sup>H. E. Huppert and J. A. Neufeld, "The fluid mechanics of carbon dioxide sequestration," *Annu. Rev. Fluid Mech.* **46**, 255–272 (2014).
- <sup>6</sup>J. Otero, L. A. Dontcheva, H. Johnston, R. A. Worthing, A. Kurganov, G. Petrova, and C. R. Doering, "High-Rayleigh number convection in a fluid-saturated porous layer," *J. Fluid Mech.* **500**, 263–281 (2004).
- <sup>7</sup>D. R. Hewitt, J. A. Neufeld, and J. R. Lister, "Ultimate regime of high Rayleigh number convection in a porous medium," *Phys. Rev. Lett.* **108**(22), 224503 (2012).
- <sup>8</sup>M. De Paoli, F. Zonta, and A. Soldati, "Influence of anisotropic permeability on convection in porous media: Implications for geological CO<sub>2</sub> sequestration," *Phys. Fluids* **28**(5), 056601 (2016).
- <sup>9</sup>A. C. Slim, "Solutorial-convection regimes in a two-dimensional porous medium," *J. Fluid Mech.* **741**, 461–491 (2014).
- <sup>10</sup>J. A. Neufeld, M. A. Hesse, A. Riaz, M. A. Hallworth, H. A. Tchelepi, and H. E. Huppert, "Convective dissolution of carbon dioxide in saline aquifers," *Geophys. Res. Lett.* **37**(22), 1–5, doi:10.1029/2010GL044728 (2010).
- <sup>11</sup>S. Backhaus, K. Turitsyn, and R. E. Ecke, "Convective instability and mass transport of diffusion layers in a Hele-Shaw geometry," *Phys. Rev. Lett.* **106**(10), 104501 (2011).
- <sup>12</sup>G. S. H. Pau, J. B. Bell, K. Pruess, A. S. Almgren, M. J. Lijewski, and K. Zhang, "High-resolution simulation and characterization of density-driven flow in CO<sub>2</sub> storage in saline aquifers," *Adv. Water Res.* **33**(4), 443–455 (2010).
- <sup>13</sup>D. R. Hewitt, J. A. Neufeld, and J. R. Lister, "Convective shutdown in a porous medium at high Rayleigh number," *J. Fluid Mech.* **719**, 551–586 (2013).
- <sup>14</sup>J. J. Hidalgo, J. Fe, L. C. Felgueroso, and R. Juanes, "Scaling of convective mixing in porous media," *Phys. Rev. Lett.* **109**(26), 264503 (2012).
- <sup>15</sup>P. Cheng, M. Besthorn, and A. Firoozabadi, "Effect of permeability anisotropy on buoyancy-driven flow for CO<sub>2</sub> sequestration in saline aquifers," *Water Resour. Res.* **48**(9), 1–16, doi:10.1029/2012WR011939 (2012).
- <sup>16</sup>C. P. Green and J. Ennis-King, "Steady dissolution rate due to convective mixing in anisotropic porous media," *Adv. Water Resour.* **73**, 65–73 (2014).
- <sup>17</sup>J. Ennis-King, I. Preston, and L. Paterson, "Onset of convection in anisotropic porous media subject to a rapid change in boundary conditions," *Phys. Fluids* **17**(8), 084107 (2005).
- <sup>18</sup>A. J. Landman and R. J. Schotting, "Heat and brine transport in porous media: The Oberbeck-Boussinesq approximation revisited," *Transp. Porous Media* **70**(3), 355–373 (2007).
- <sup>19</sup>C. W. MacMinn, J. A. Neufeld, M. A. Hesse, and H. E. Huppert, "Spreading and convective dissolution of carbon dioxide in vertically confined, horizontal aquifers," *Water Resour. Res.* **48**(11), 1–11, doi:10.1029/2012WR012286 (2012).
- <sup>20</sup>S. Pramanik and M. Mishra, "Coupled effect of viscosity and density gradients on fingering instabilities of a miscible slice in porous media," *Phys. Fluids* **28**(8), 084104 (2016).
- <sup>21</sup>F. Zonta and A. Soldati, "Effect of temperature dependent fluid properties on heat transfer in turbulent mixed convection," *J. Heat Transfer* **136**(2), 022501 (2014).
- <sup>22</sup>F. Zonta, C. Marchioli, and A. Soldati, "Modulation of turbulence in forced convection by temperature-dependent viscosity," *J. Fluid Mech.* **697**, 150–174 (2012).
- <sup>23</sup>M. Bickle, A. Chadwick, H. E. Huppert, M. Hallworth, and S. Lyle, "Modelling carbon dioxide accumulation at Sleipner: Implications for underground carbon storage," *Earth Planet. Sci. Lett.* **255**(1), 164–176 (2007).
- <sup>24</sup>X. Xu, S. Chen, and D. Zhang, "Convective stability analysis of the long-term storage of carbon dioxide in deep saline aquifers," *Adv. Water Resour.* **29**(3), 397–407 (2006).
- <sup>25</sup>A. C. Slim and T. S. Ramakrishnan, "Onset and cessation of time-dependent, dissolution-driven convection in porous media," *Phys. Fluids* **22**(12), 124103 (2010).
- <sup>26</sup>A. C. Slim, M. M. Bandi, J. C. Miller, and L. Mahadevan, "Dissolution-driven convection in a Hele-Shaw cell," *Phys. Fluids* **25**(2), 024101 (2013).
- <sup>27</sup>M. A. Hesse, "Mathematical modeling and multiscale simulation for CO<sub>2</sub> storage in saline aquifers," Ph.D. thesis, Department of Energy Resources Engineering, Stanford University, 2008.
- <sup>28</sup>D. R. Hewitt, J. A. Neufeld, and J. R. Lister, "High Rayleigh number convection in a three-dimensional porous medium," *J. Fluid Mech.* **748**, 879–895 (2014).